

## Supplementary Materials for

### **Sculpted grain boundaries in soft crystals**

Xiao Li, José A. Martínez-González, Orlando Guzmán, Xuedan Ma, Kangho Park, Chun Zhou, Yu Kambe, Hyeon Min Jin, James A. Dolan, Paul F. Nealey\*, Juan J. de Pablo\*

\*Corresponding author. Email: [nealey@uchicago.edu](mailto:nealey@uchicago.edu) (P.F.N.); [depablo@uchicago.edu](mailto:depablo@uchicago.edu) (J.J.d.P.)

Published 29 November 2019, *Sci. Adv.* **5**, eaax9112 (2019)  
DOI: 10.1126/sciadv.aax9112

#### **The PDF file includes:**

Continuum simulations  
Estimation of the grain boundary free energies  
Fig. S1. Pattern characteristics.  
Fig. S2. Schematic for estimating the grain boundary energies.  
Fig. S3. Grain boundary variation during phase transition by heating.  
Fig. S4. Lateral dimension of grain boundary.  
Fig. S5. Binary array pattern during phase transitions by thermal process.  
Fig. S6. Martensitic transformations during cooling process.  
Fig. S7. Simulated optical diffraction patterns.  
Legend for movie S1  
References (31–33)

#### **Other Supplementary Material for this manuscript includes the following:**

(available at [advances.sciencemag.org/cgi/content/full/5/11/eaax9112/DC1](https://advances.sciencemag.org/cgi/content/full/5/11/eaax9112/DC1))

Movie S1 (.mp4 format). C-shaped grain-boundary under electric field.

## Supplementary Notes

### Continuum simulations

Mean-field Landau-de Gennes approach. In this model, the free energy,  $F$ , of the chiral liquid crystal is given by  $F=F(\mathbf{Q})$ , where  $\mathbf{Q}$  is the tensor order parameter, which contains the information about the morphology adopted by the material and is defined by  $Q_{ij}=S (n_i n_j -1/3 \delta_{ij})$ , where  $S$  is the scalar order parameter,  $n_i$  are the components of the local director vector ( $i, j =1,2,3$ ).  $F(\mathbf{Q})$  accounts for short-range ( $f_{\text{LdG}}$ ), long-range elastic ( $f_E$ ) and surface ( $f_s$ ) contributions, i. e.

$$F(\mathbf{Q}) = \int d^3x [f_{\text{LdG}}(\mathbf{Q}) + f_E(\mathbf{Q})] + \int d^2x f_s(\mathbf{Q}) \quad (1)$$

where the short-range contribution, ( $f_{\text{LdG}}$ ), reads

$$f_{\text{LdG}} = \frac{A}{2} \left(1 - \frac{U}{3}\right) \text{tr}(\mathbf{Q}^2) - \frac{AU}{3} \text{tr}(\mathbf{Q}^3) + \frac{AU}{4} \text{tr}(\mathbf{Q}^2)^2 \quad (2)$$

where  $A$  and  $U$  are parameters that depend on pressure and temperature (31). The second term in Eq. 1 accounts for the elastic contribution and is given by

$$f_E = \frac{1}{2} \left[ L_1 \frac{\partial Q_{ij}}{\partial x_k} \frac{\partial Q_{ij}}{\partial x_k} + L_2 \frac{\partial Q_{jk}}{\partial x_k} \frac{\partial Q_{jl}}{\partial x_l} + L_3 Q_{ij} \frac{\partial Q_{kl}}{\partial x_i} \frac{\partial Q_{kl}}{\partial x_j} + L_4 \frac{\partial Q_{jk}}{\partial x_l} \frac{\partial Q_{jl}}{\partial x_k} + L_5 2q_0 \epsilon_{ikl} Q_{ij} \frac{\partial Q_{lj}}{\partial x_k} \right] \quad (3)$$

where  $L_i$ 's are the elastic constants of the liquid crystal,  $\varepsilon_{ikl}$  is the Levi-Civita tensor,  $p$  is the pitch and  $q_0=2\pi/p$  measures the chirality of the system.

The last term of Eq. 1 accounts for the surface contributions to the free energy. For planar degenerate anchoring, we have (32)

$$f_S^P = W_P(\tilde{\mathbf{Q}} - \tilde{\mathbf{Q}}^\perp)^2 + W_P(\tilde{\mathbf{Q}} : \tilde{\mathbf{Q}} - S_0^2)^2 \quad (4)$$

Where  $W_P$  is the planar anchoring energy,  $S_0$  is the surface preferred degree of order,  $\tilde{\mathbf{Q}} = \mathbf{Q} + SI/3$  and  $\tilde{\mathbf{Q}}^\perp = \mathbf{P}\tilde{\mathbf{Q}}\mathbf{P}$ ,  $\mathbf{P}$  is the projection operator  $P_{ij} = \delta_{ij} - v_i v_j$  and  $\mathbf{v}$  is the vector normal to the surface. For homeotropic anchoring, the surface free energy is

$$f_S^H = \frac{1}{2}W_H(\mathbf{Q} - \mathbf{Q}^0)^2 \quad (5)$$

where  $W_H$  is the homeotropic anchoring energy and  $\mathbf{Q}^0$  is a surface-preference tensor order parameter. In this work, the patterned surfaces correspond to combinations of planar and homeotropic regions, where each one contributes to the surface free energy according Eq. 4 and 5, respectively.

Stable and metastable states were found by minimization of the free energy following the Ginzburg-Landau relaxation method where  $\mathbf{Q}$  evolves toward equilibrium according to (31)

$$\frac{\partial \mathbf{Q}}{\partial t} = -\frac{1}{\gamma} \left[ \mathbf{\Pi} \left( \frac{\delta F}{\delta \mathbf{Q}} \right) \right] \quad (6)$$

with boundary conditions such that  $\mathbf{\Pi}[(\delta F/\delta \nabla \mathbf{Q}) \cdot \mathbf{v}] = 0$ . In Eq. 6, the parameter  $\gamma$  represents a diffusion coefficient and the operator  $\mathbf{\Pi}(\mathbf{B}) = 1/2 (\mathbf{B} + \mathbf{B}^T) - 1/3 \text{tr}(\mathbf{B}) \mathbf{I}$  ensures the symmetric and traceless properties of the  $\mathbf{Q}$ -tensor parameter.

Initial configurations for BPII were generated by the following ansatzes (33)

$$Q_{xx} = A (\cos kz - \cos ky) \quad (8a)$$

$$Q_{xy} = A \sin kz \quad (8b)$$

The components  $yy$ ,  $zz$ ,  $xz$  and  $yz$  were obtained by cyclic permutation of those given above;  $k$  depends on the chirality according to  $k=2q_0r$ , where  $r$  is the redshift. The amplitude of initialization is  $A=0.2$ .

For the description of the system we use a lattice array with a mesh resolution of 7.5 nm,  $W_P = 4 \times 10^{-3} \text{ Jm}^{-2}$  and  $W_H = 8 \times 10^{-4} \text{ Jm}^{-2}$ ; for the chiral liquid, we use the following values, which were found to match experimental observations (13, 19),  $A=1.067 \times 10^5 \text{ Jm}^{-3}$ ,  $L_I=6 \text{ pN}$  and  $L_5=2L_1$ .  $p = 258 \text{ nm}$  and  $U=2.755$ . For simulations, reduced variables are obtained by  $r^*=r/\xi_C$ ,  $W^*= \xi_C/\xi_S$  and  $F^*=F/(L_1\xi)$ , where  $\xi_C = \sqrt{L_1/A}$  is the coherence length and  $\xi_S = L_1/W$ , is known as the extrapolation length.

## Estimation of the grain boundary free energies

We can interpret our observations in terms of a competition between substrate-induced and grain-boundary contributions to the total free energy of the system. We compare the free energy of an heterogeneous system (with a  $\text{BPII}_{(110)}$  domain over a rectangular-pattern substrate and a  $\text{BPII}_{(100)}$  domain over a stripe-pattern substrate) with that of an homogeneous system (with a monodomain of  $\text{BPII}_{(110)}$  over both types of substrate). Our model for the heterogeneous system consists of a periodic array of slabs with alternating widths  $w_{\text{RP}}$  and  $w_{\text{SP}}$  (see fig. S2 A and B).

We consider a representative region with width  $X = w_{\text{RP}} + w_{\text{SP}}$ , lateral size  $Y$ , and film thickness  $Z$ . In a previous work (19), the bulk free energy of each  $\text{BPII}$  orientation was calculated by mean-field-theory simulations and found to differ over different types of anchoring condition patterns, therefore establishing which orientation is the most stable over a particular substrate pattern. While the origin of such differences is the interaction of the liquid crystal with the underlying substrate, the free energy contribution of the particular configuration of double twist cylinders that conforms to the anchoring conditions specified by the substrate is associated with a three-dimensional region above the substrate.

We can model this free energy contribution as a sum of idealized volumetric and surface contributions. For the heterogeneous system, the surface contributions due to the grain boundary are proportional to the contact area  $A = YZ$ , while those due to the substrate-BP interfaces are proportional to the areas  $w_{\text{RP}} Y$  or  $w_{\text{SP}} Y$

$$\begin{aligned}
F_{het} &= \int f(r)dr^3 + \int \gamma(r)dr^2 \\
&= f_{\frac{110}{RP}} w_{RP}YZ + f_{\frac{100}{SP}} w_{SP}YZ \\
&\quad + \gamma_{\frac{110}{RP}} w_{RP}Y + \gamma_{\frac{100}{SP}} w_{SP}Y + 2 \gamma_{\frac{110}{RP}|\frac{100}{SP}} YZ
\end{aligned} \tag{9}$$

where  $f_{\frac{o}{s}}$  represents the substrate-induced free-energy density of orientation  $o = (100), (110)$  or  $(111)$  covering substrate  $s = SP, RP$  or  $CP$ , while  $\gamma_{\frac{110}{RP}|\frac{100}{SP}}$  represents the grain-boundary free-energy density associated to  $BPII_{(100)}$  over  $SP$  meeting  $BPII_{(110)}$  over  $RP$ .

Analogously, for the homogeneous system

$$\begin{aligned}
F_{hom} &= \int f(r)dr^3 + \int \gamma(r)dr^2 \\
&= f_{\frac{110}{RP}} w_{RP}YZ + f_{\frac{110}{SP}} w_{SP}YZ \\
&\quad + \gamma_{\frac{110}{RP}} w_{RP}Y + \gamma_{\frac{110}{SP}} w_{SP}Y
\end{aligned} \tag{10}$$

as, for this case, there are no grain boundaries. Then, we find for the free energy difference per unit area  $\Delta F/A = (F_{het} - F_{hom})/A$

$$\frac{\Delta F(w_{SP})}{A} = - \left( \left[ f_{\frac{110}{SP}} + \frac{\gamma_{\frac{110}{SP}}}{Z} \right] - \left[ f_{\frac{100}{SP}} + \frac{\gamma_{\frac{100}{SP}}}{Z} \right] \right) w_{SP} + 2 \gamma_{\frac{110}{RP}|\frac{100}{SP}} \tag{11}$$

If we define “renormalized” free energy densities

$$f'_{\frac{110}{SP}} = f_{\frac{110}{SP}} + \frac{\gamma_{\frac{110}{SP}}}{Z} \quad (12a)$$

$$f'_{\frac{100}{SP}} = f_{\frac{100}{SP}} + \frac{\gamma_{\frac{100}{SP}}}{Z} \quad (12b)$$

which remain constant for experiments performed with the same film thickness  $Z$ , we obtain

$$\frac{\Delta F(w_{SP})}{A} = - \left[ f'_{\frac{110}{SP}} - f'_{\frac{100}{SP}} \right] w_{SP} + 2 \gamma_{\frac{110}{RP} | \frac{100}{SP}} \quad (13)$$

Since (100) is more stable than (110) over the SP region,  $\Delta f_{SP} \equiv f_{\frac{110}{SP}} - f_{\frac{100}{SP}} > 0$ . The

heterogeneous state is stable only when  $\frac{\Delta F(w_{SP})}{A} < 0$ , which occurs for

$$w_{SP} > w_{SP}^{min} = 2 \frac{\gamma_{\frac{110}{RP} | \frac{100}{SP}}}{\Delta f_{SP}} \quad (14)$$

From this expression, we arrive at an estimate for  $\gamma_{\frac{110}{RP} | \frac{100}{SP}}$  : using the value  $\Delta f_{SP} \sim 1 \text{ Jm}^{-3}$

(obtained from simulations (19) and the measured value  $w_{SP}^{min} \sim 10 \text{ } \mu\text{m}$ , we find  $\gamma_{\frac{110}{RP} | \frac{100}{SP}} = 5 \times 10^{-6}$

$\text{Jm}^{-2}$ . Knowing  $\gamma_{\frac{110}{RP} | \frac{100}{SP}}$  we can calculate an effective elastic constant  $K_{\text{eff}}$  associated with

gradients of orientation in BPs. Assuming that such changes occur over distances on the order of

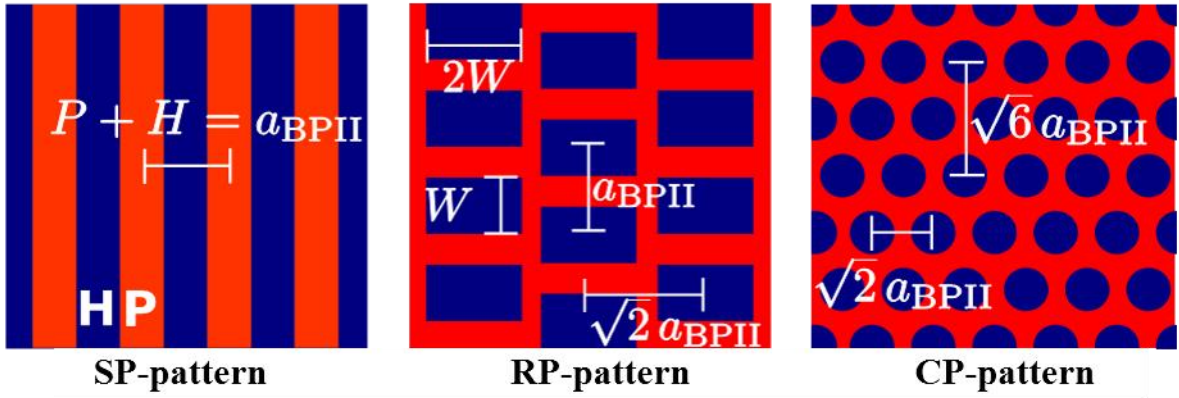
the unit-cell size,  $\Delta x = 150 \text{ nm}$ , the grain-boundary free-energy density would be  $\gamma_{\frac{110}{RP} | \frac{100}{SP}} \sim$

$K_{\text{eff}}/\Delta x$ . Solving for the elastic constant we arrive at  $K_{\text{eff}} \sim 10^{-12}$  N, which is of the same order of magnitude than the elastic constants of low-molecular-weight thermotropic materials.

For large thickness  $Z$ , the renormalized  $f^*$  tends to the unnormalized  $f$ . For values  $f \sim 1 \text{ Jm}^{-3}$  of the order of those obtained by computer simulation and for values  $\gamma \sim 10^{-6} \text{ Jm}^{-2}$  of the order of interfacial energies of low-molecular weight liquid crystals, demanding  $f \gg \gamma/Z$  requires a thickness  $Z \gg 1 \text{ }\mu\text{m}$ . In order to measure the surface free energy difference  $\gamma_{\frac{100}{SP}} - \gamma_{\frac{110}{SP}}$  for different orientations over the same substrate, one could analyze the results from experiments performed at increasing values of film thickness  $Z$ .



### A Pattern Designs



### B SEM Images

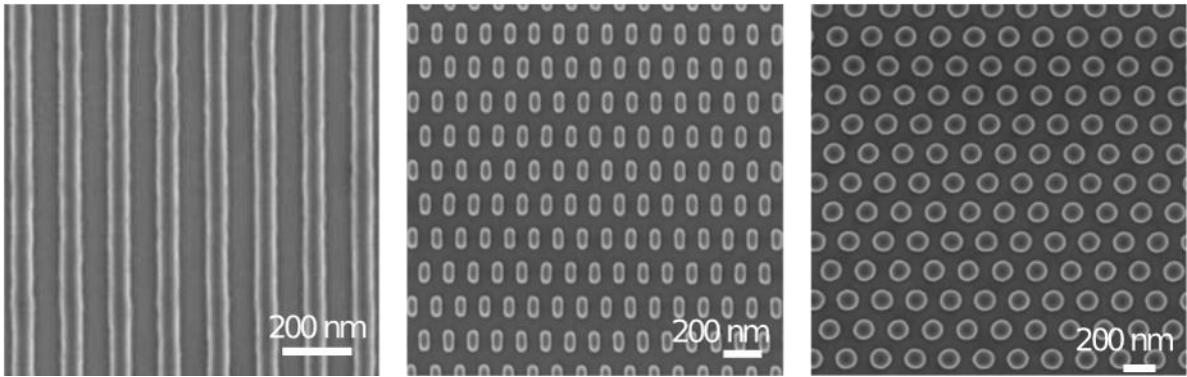


**Fig. S1. Pattern characteristics.** A) Pattern designed for SP (stripe pattern), RP (rectangular pattern) and CP (circular pattern) patterns. B) SEM images for the each one of the patterns considered.

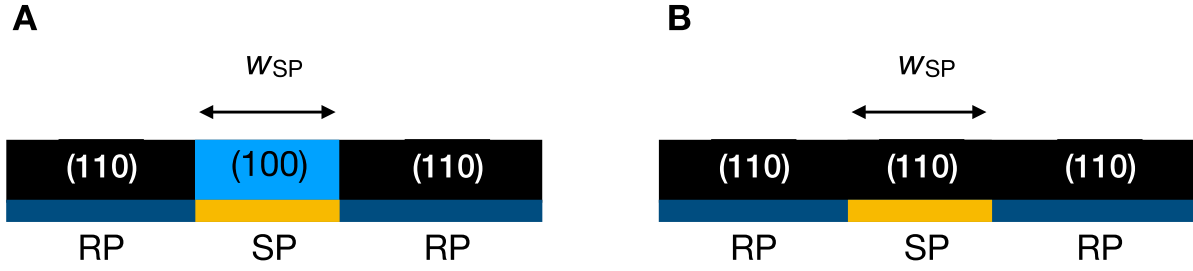


**Fig. S2. Schematic for estimating the grain boundary energies.** The stability condition of the heterogenous configuration **A** was obtained by comparing its free energy with that of the homogenous state **B** in terms of the width  $w_{SP}$  of the SP region. In our analysis, we assume periodic boundary conditions for configurations **A** and **B**.

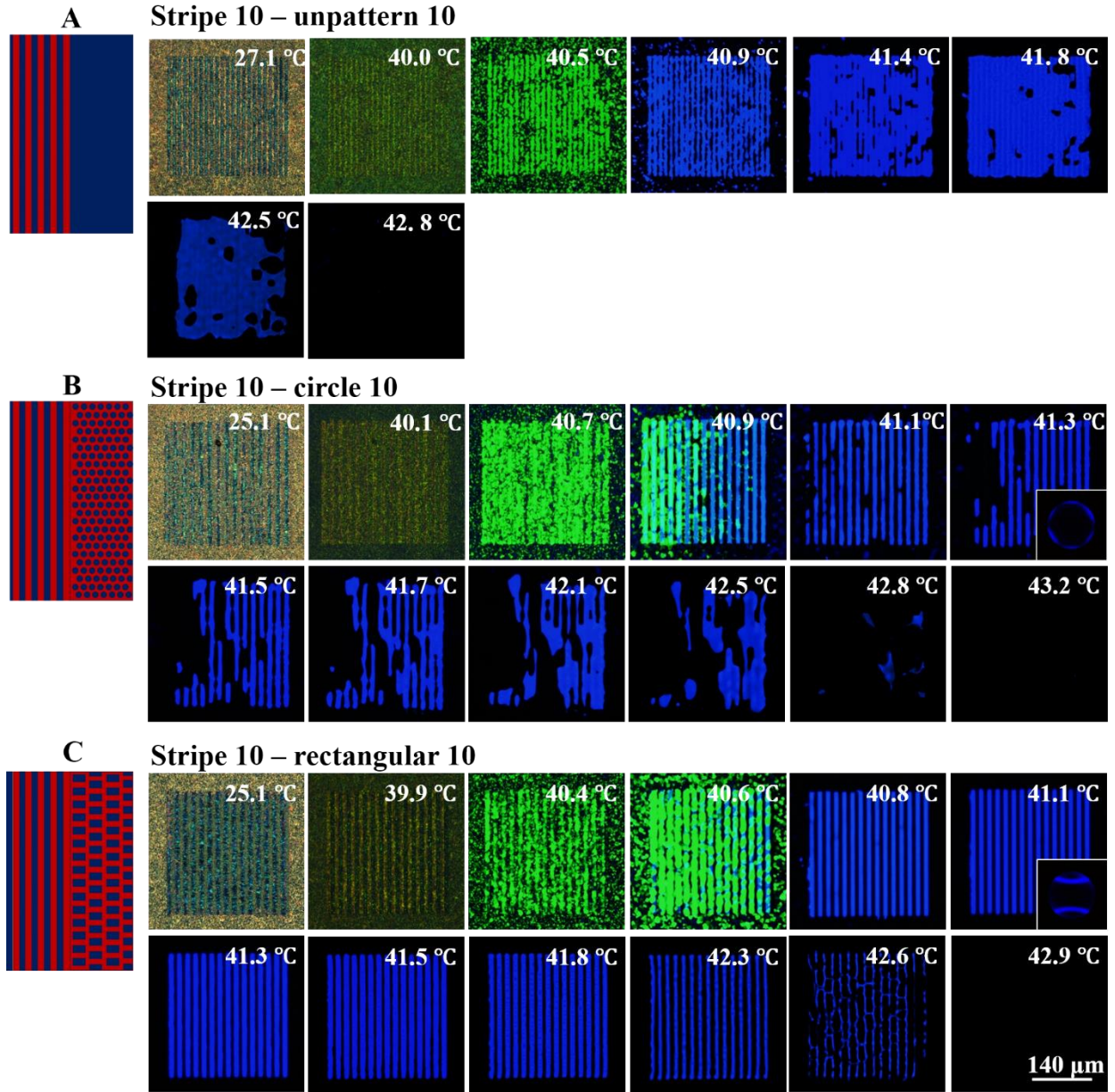


**Fig. S3. Grain boundary variation during phase transition by heating.** Reflection optical microscopy images of the system at different temperature upon heating process for A) SP-H array, B) SP-CP array and C) for SP-RP array.



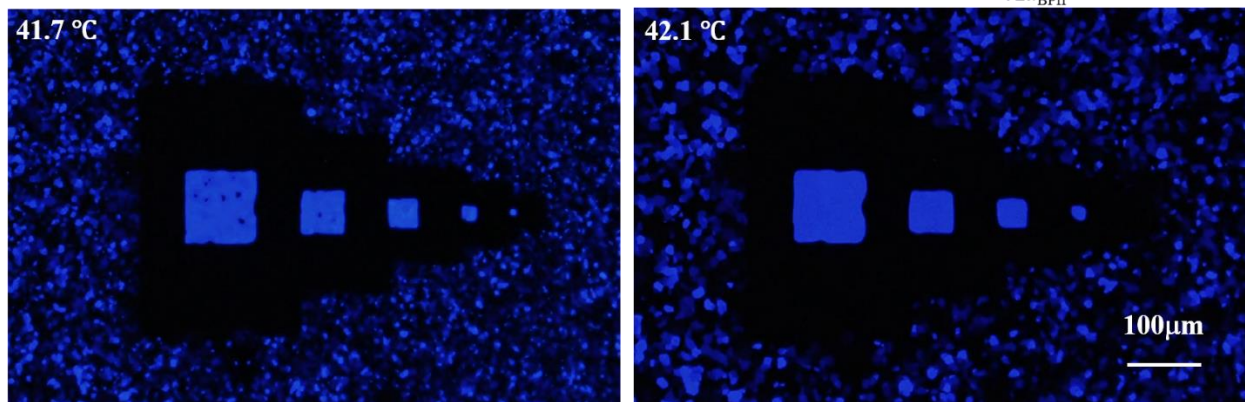
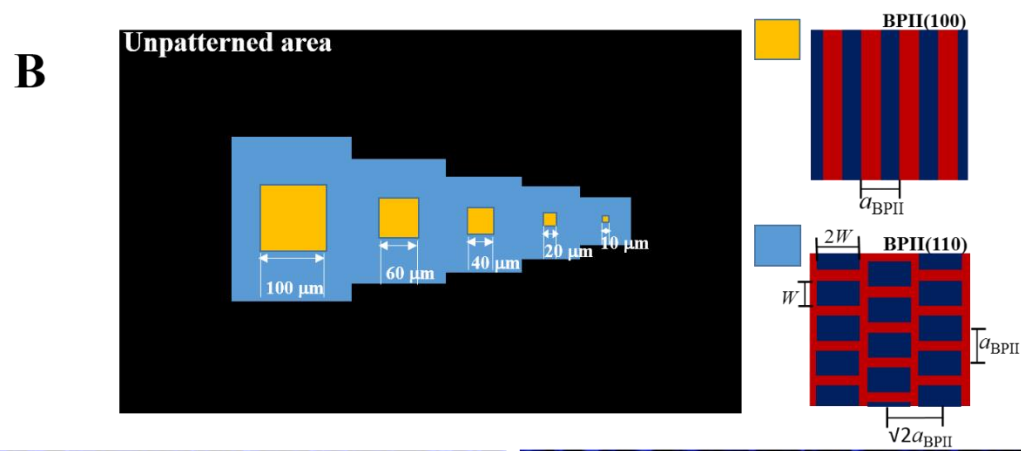
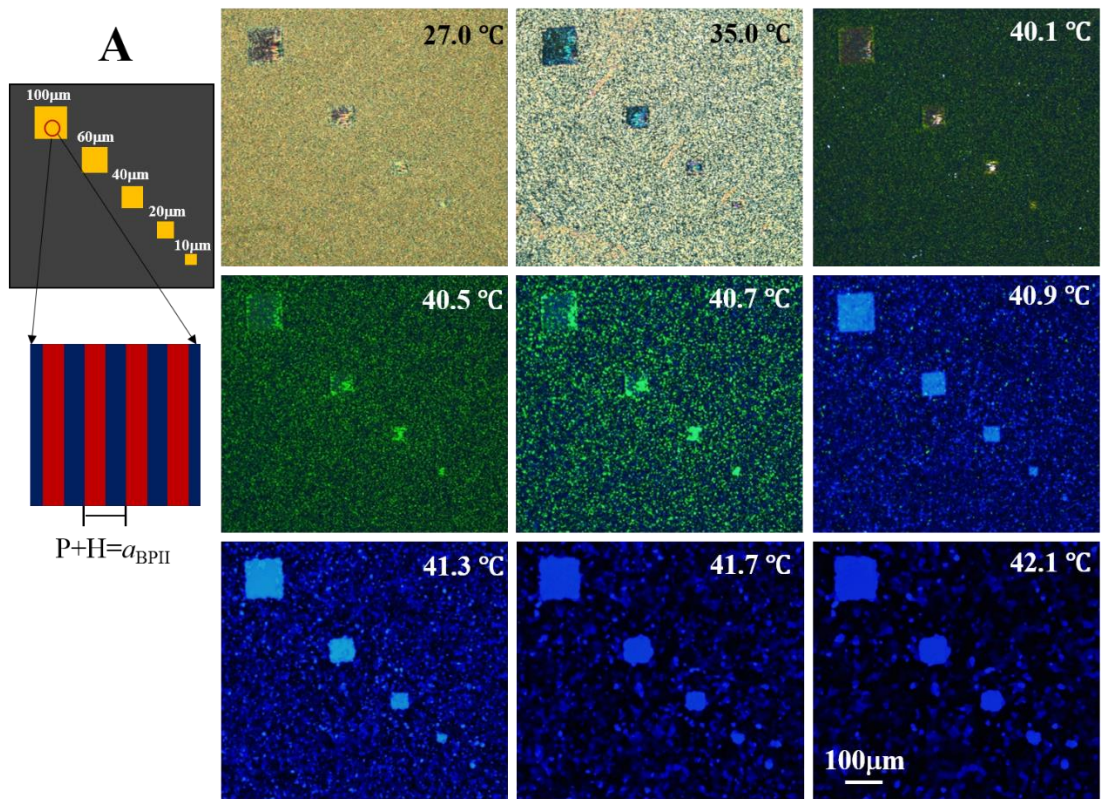


**Fig. S4. Lateral dimension of grain boundary.** Schematics and reflection optical microscopy images of BP transition on (A) stripe pattern surface with different total pattern size: 100  $\mu\text{m}$ , 60  $\mu\text{m}$ , 40  $\mu\text{m}$ , 20  $\mu\text{m}$ , 10  $\mu\text{m}$  according to different temperature upon heating process. (B) Stripe pattern surface surrounding by rectangular pattern regions at two temperatures during a heating process, where the stripe pattern size regions vary: 100  $\mu\text{m}$ , 60  $\mu\text{m}$ , 40  $\mu\text{m}$ , 20  $\mu\text{m}$ , and 10  $\mu\text{m}$ .

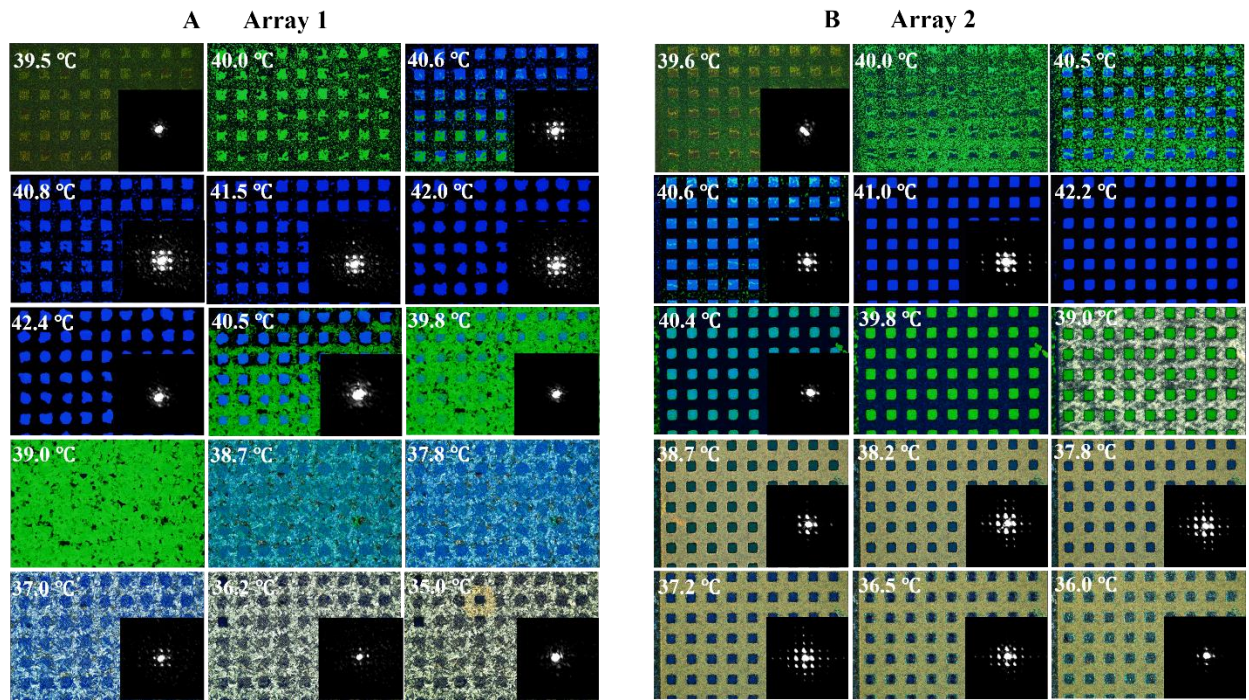
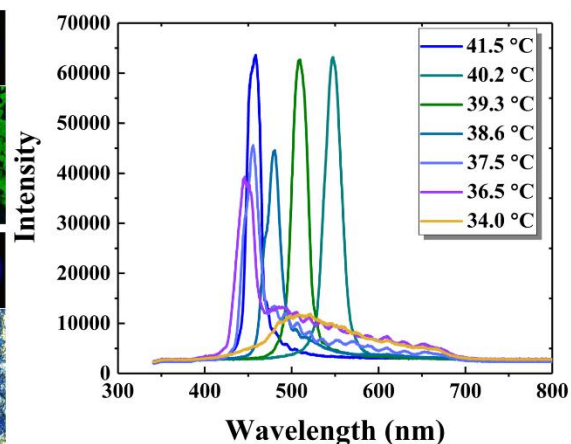
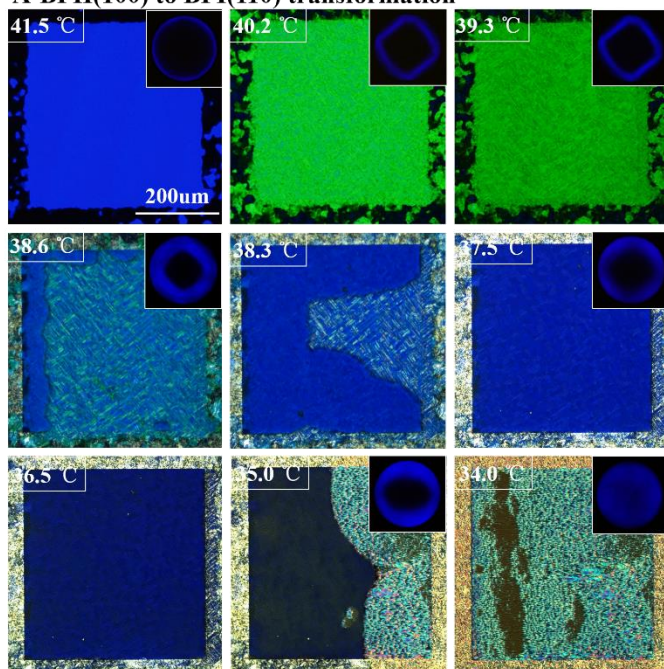


**Fig. S5. Binary array pattern during phase transitions by thermal process.** Reflection optical microscopy images of the system Array 1 (A) and Array 2 (B), with their corresponding diffraction patterns at different temperatures during both heating and cooling process.



### A-BPII(100) to BPI(110) transformation



### B-BPII(110) to BPI(200) transformation

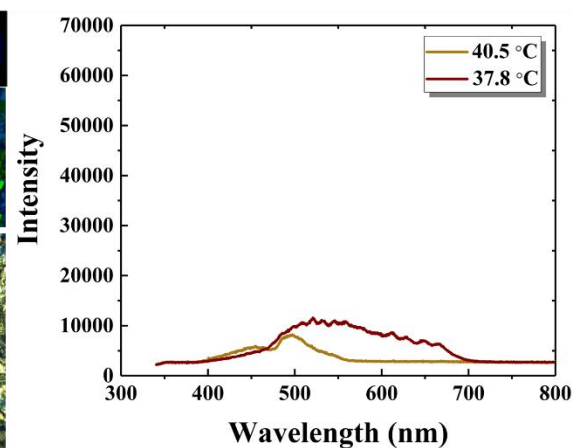
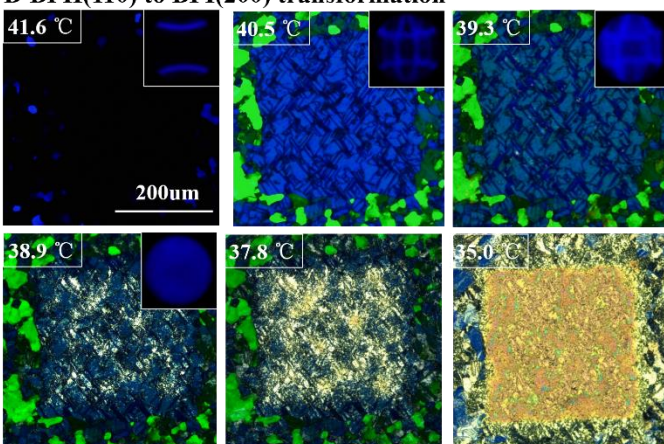
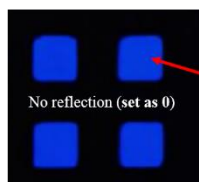


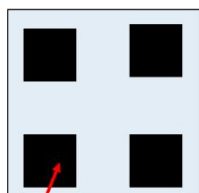
**Fig. S6. Martensitic transformations during cooling process.** Reflection optical microscopy images of BP materials on stripe (A) and rectangular (B) patterned surface during the cooling process, and the corresponded spectrometer and Kossel diagram have been inserted in each image.

## A POM image



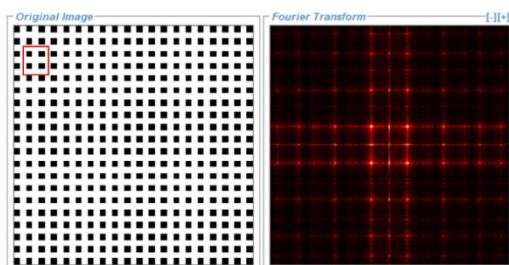
Maximum  
Reflection (set as 1)

## Unit cell (sharp border)

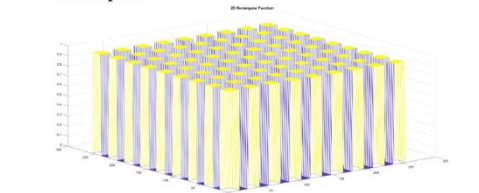


Maximum reflection from BPII

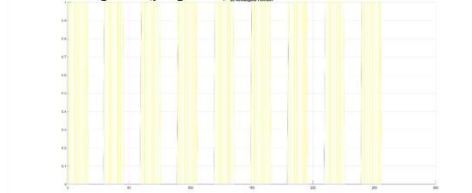
## FFT



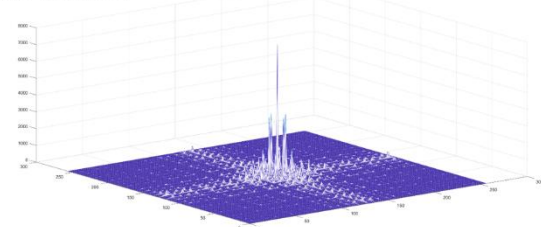
## Real space



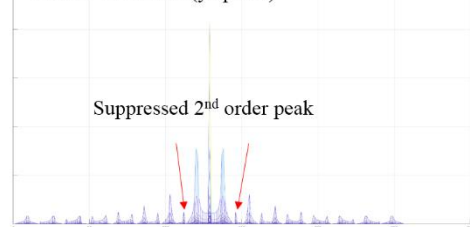
## Real space (yz plane)



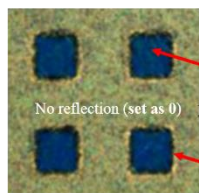
## Fourier Transform



## Fourier Transform (yz plane)



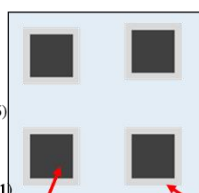
## B POM image



Relatively high  
Reflection (set as 0.6)

Weak  
Reflection (set as 0.1)

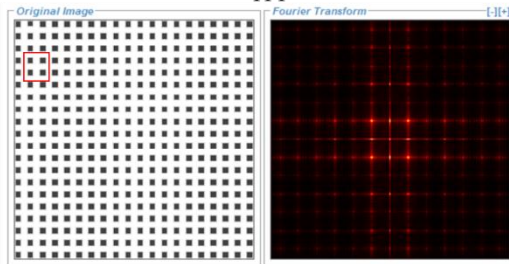
## Unit cell (broad border line)



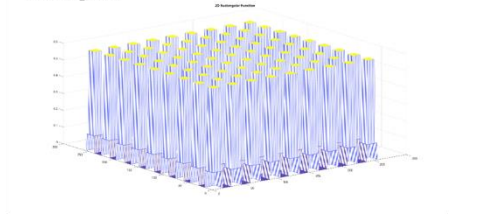
Relatively high  
reflection  
from chol.

Broad border  
line with  
weak reflection

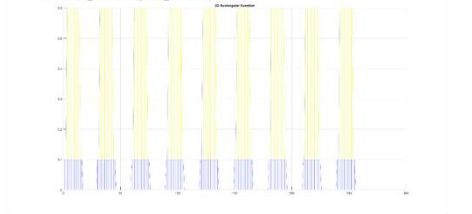
## FFT



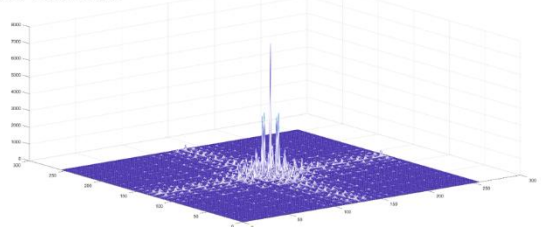
## Real space



## Real space (yz plane)



## Fourier Transform



## Fourier Transform (yz plane)

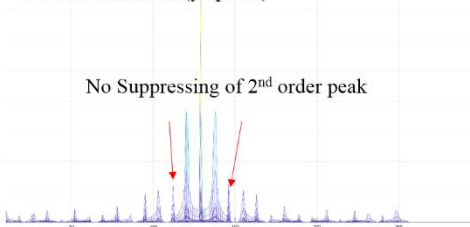


**Fig. S7. Simulated optical diffraction patterns.** The 2D diffraction pattern from array2 observed at temperature range (41.0 and 37.8°C) after a cooling process. For the BP<sub>II</sub> regime, such diffraction patterns are well defined. At the Chol regime, the uniform color is from the well aligned cholesteric phase by nano-stripe pattern. The 2<sup>nd</sup> order peaks show up because of the form factor contribution to the diffraction pattern, as shown in the real space and Fourier Transform images.

**Movie S1. C-shaped grain-boundary under electric field.** The BP system was kept at 39.8 °C (within the BPI domain), then an external electric field (3.5V) was applied between two electrodes on the conductive Si-substrate to trigger the martensitic-like transformation from BPI to BP<sub>II</sub>; once the electric field was switch off, the martensitic-like transformation from BP<sub>II</sub> to BPI was observed.